

# Experimental and numerical investigation of a turbulent lobed diffuser jet: application to residential comfort

Abderazak Bennia<sup>1,\*</sup>, Larbi Loukarfi<sup>1</sup>, Ali Khelil<sup>1</sup>, Said Mohamadi<sup>2</sup>, Mohamed Braikia<sup>1</sup>, and Hassan Najji<sup>3</sup>

<sup>1</sup> Laboratoire de Contrôle, Essai, Mesure et Simulation Mécaniques, Université Hassiba Benbouali de Chlef, Hay Salem, route nationale No 19, 02000 Chlef, Algeria

<sup>2</sup> Laboratoire de Mécanique des Fluides Théorique et Appliquée, Université des Sciences et Technologie, Houari Boumediene Bab Ezzouar, Alger 16111, Algérie

<sup>3</sup> University of Artois & Lille University Northern France, LGCgE, Technoparc Futura, 62400 Béthune, France

Received: 19 October 2015 / Accepted: 8 December 2016

**Abstract.** In this work, we present an experimental and numerical study of a turbulent jet from a lobed diffuser, applied to residential comfort. The main aim is the improvement of the air diffusion efficiency, of the ventilation driving flow in the occupancy zone, with least cost. The experiments have been conducted in a room where the dimensions enable a better execution in the conditions of free and hot vertical jet at unfavorable pushing forces. The room has been isolated from the environment during experiments. The temperature difference between the jet and the environment has been controlled by readjusting the blowing jet temperature. Consequently, the jet's Archimedes number is kept constant during tests. The installation includes a hot air blowing diffuser oriented from top to bottom. The temperatures and velocities of the flow have been measured by a multi-functional thermo-anemometer. The probe is supported by a stem that is guided vertically and horizontally in order to sweep a maximum space. The numerical study has been carried out using the Fluent code (V.6). The numerical results obtained with the turbulence model (RNG  $k-\epsilon$ ) turned out to be in a good accordance with the experimental results.

**Keywords:** Lobed jet / thermal homogenization / comfort / experimental study / numerical simulation / turbulence modelling

## 1 Introduction

The mixing processes are intimately related to the turbulence transition [1,2]. The geometry and initial perturbations of the flow strongly influence both its generation and its transition [1]. The applications of mixing via jets are numerous. These include the thrust force of plane reactors, the dispersion of pollutants, heating, ventilation and air conditioning used in habitation [1,2]. In addition, a good spatial distribution of the air low rate to be injected is necessary in residences, for a best users' comfort [1].

In order to improve the air diffusion efficiency at least cost, taking account of the esthetic aspect in the design of the air diffusion terminal units, we propose a "passive" way, which consists of blowing the jet through a lobed diffuser. So far, such geometry has proved effective in the aeronautic and aerospace fields. They are introduced in the design of the ejectors placed on reactor outputs. They are also used in the combustion domain and in the design of injectors

offering a good combustion stability [3–6]. This passive control enables the improvement of the air diffusion in the building [7].

The observed induction gain is produced without reduction in the jet range. This is because of the flow acceleration which is due to the vein contraction at the blowing exit [3–6]. Large secondary structures, developed in the trough of the lobed nozzle, give an apparent rotation effect to the flow. The axes crossing phenomenon participates to increase in the induction performance of the lobed jet. It is also possible to optimize the elementary lobed orifice geometry of the diffuser in order to improve the global performance [3,5].

It should be noted that the objective of works conducted at LEPTIAB (Laboratoire des phénomènes de transfert et d'instantanéité: Agro-ressources et bâtiment) since 2003 on jets passive control is to transpose the "asymmetric diffuser" idea from aeronautics and combustion to that of the air diffusion in buildings [3,4,6,8–12]. Therefore, the Reynolds number is relatively important, the jet is often confined and the zone of interest is short and sometimes limited to the potential core.

\* e-mail: [Abderazak.Bennia@USherbrooke.ca](mailto:Abderazak.Bennia@USherbrooke.ca)

Even if the data available in the literature are qualitative or limited to the application of air diffusion in living spaces, they remain nonetheless valuable to help choose efficient geometries for better integration into air diffusion terminal units. It is this observation that motivated this study which aims to study the lobed jets which allow testing the geometries in conditions consistent with the application intended.

Yuan [13] was among the first to be interested in the circular lobe nozzle effect of different shapes and with a variable number of lobes. He showed that increasing the lobe width has no significant effect on the dynamic field, and at a constant section, rising the lobes' number reduces the lobe width. In addition, this author has shown that this yields a blocking of the swirling circulation probably unfavorable to the entrainment. To the work achieved by Yuan [13], those of Hu et al. [14,15] may be added. Unlike the previous boundary conditions (BCs), the air jet here is free and diffuse in the air at rest. Note that for these experiments, the initial Reynolds number  $Re_{0C}$ , based on the nozzle equivalent diameter and the central blowing velocity  $U_{0C}$  of  $1.2 \text{ m}\cdot\text{s}^{-1}$ , is equal to 3000 [14,15].

Bennia et al. [16] presented an experimental study of a turbulent jet with a lobed diffuser for winter comfort in residences. The sighted objective is to improve the efficiency of the air diffusion in the occupation zone at a least cost by a passive control way of the ventilation driving flow. A comparative study of the performance of different types of jets has been conducted. By analyzing the jet axial temperature profiles for 20 equivalent diameters, a comparison, between the lobed diffuser with a wide opening and at low height and the diffuser with and without swirling, shows that the lobed jet, in similar blowing conditions, provides better stability of radial temperatures, while the swirl jet inclined at  $60^\circ$  ensures better radial temperature spreading.

In addition, Bennia et al. [17] conducted a comparative study on the performance of different nozzle geometries. By analyzing jet axial velocity profiles, the comparison of the lobed jet using various lobe geometries shows that an inclined-lobe diffuser homogenizes the air flow in the experimental room relatively better than a lobed diffuser with a right section. Furthermore, at low height, the diffuser having wide opening lobes proved to be more efficient. Moreover, the use of the lobed jet, under similar blowing conditions of that of the swirling jet, showed an improvement of the air flow thermal homogenization.

Meslem et al. [12] studied the performances of three turbulence models, viz. the shear stress transport (SST)  $k-\omega$ , RSM, and the standard  $k-\varepsilon$  models. They noted that none of the turbulence models can properly predict all flow characteristics. However, it has been shown that it is the turbulence model SST  $k-\omega$  that is able to correctly predict jets interaction, global dynamic expansion, and entrainment of the ambient air for the rate flow from the lobed diffuser.

Meslem et al. [18] have also highlighted the experimental validation complexity of a three-dimensional flow. They showed that the SST  $k-\omega$  model provides the best prediction

of dynamic parameters useful for optimizing the lobed orifice geometry with respect to its induction capacity. It appears from their analysis of the turbulent field that no turbulence models correctly reproduce turbulent kinetic energy. Unlike the  $k-\omega$  and SST  $k-\omega$  models, the RSM and  $k-\varepsilon$  models predict non-physical growth of this quantity at the blow-out. This explains the wrong prediction of the rate flow by these two models.

In a previous study, Meslem et al. [19] investigated a free lobed jet at a moderate Reynolds number to optimize an air diffuser for heating, ventilation, and air conditioning systems. They leaned on experimental data of a jet issued from a cross-shaped orifice [5] to assess the prediction of seven turbulence models. It appears that none of the turbulence models is able to simultaneously predict all the jet characteristics. Specifically, the SST  $k-\omega$  model underestimated the jet spread and induction of ambient air, while poorly assessing the transverse deformation of the jet. In addition, the turbulences increase the kinetic energy in the near field of the jet for  $k-\varepsilon$  turbulence and RSM models. In this region, the SST  $k-\omega$  model was in good agreement with the measurements.

The principal objective of the present work is to study, temperatures distribution, experimentally and numerically. It is the "Fluent" code that has selected to perform such a simulation. It should be noted that this kind of flow has been considered here because of its wide application during residential ventilation.

## 2 Experimental device

The experimental setup has been primarily designed to generate an air jet from a lobed diffuser. The experiments were achieved in a room having a length of 3.0 m, a width of 2.5 m, and a height of 2.5 m. This choice enables to perform tests in a vertical jet and hot jet conditions with unfavorable pressure forces. The room was isolated from the environment during the tests. Due to the non-thermal control of the room walls, the temperature was not kept constant.

It will be noted that the temperature difference between the jet and the environment is thereby controlled by a readjustment of the blowing air jet temperature. As a result, the Archimedes number of the jet is kept constant over the experiments.

The setup consists of a chassis on which the blowing device is fixed (Fig. 1). The latter includes a downward-facing hot air blowing diffuser. The flow temperatures are measured with a multifunctional thermo-anemometer. The probe is supported vertically and horizontally by rod guides to sweep a maximum space. The calibration tolerance of the portable anemometer device for temperature is  $\pm 0.5^\circ\text{C}$  [20]. A digital thermometer is placed outside the flow in the test room to instantly measure the ambient air temperature ( $T_a$ ). The experimental measurement devices in the free mode are shown in Figure 1. The ambient temperature  $T_a$  and the temperature of the jet  $T_i$ , at different points, are measured simultaneously.

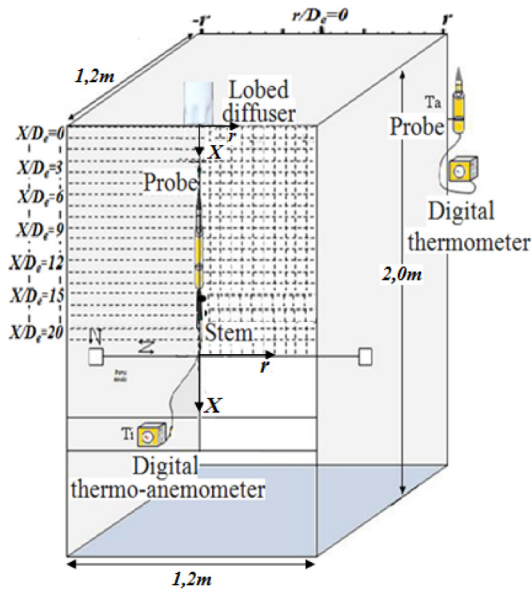


Fig. 1. Sketch of the experimental setup.

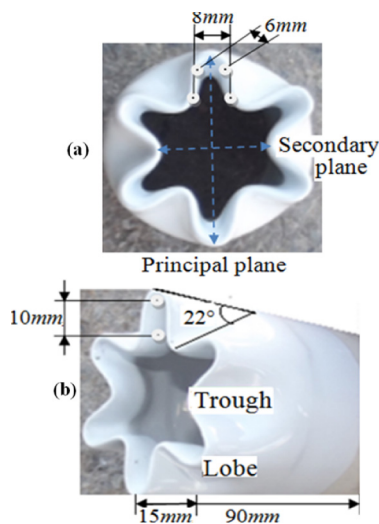


Fig. 2. (a) Blowing plane geometry (YZ), (b) lobes nozzle photography.

Figure 2 shows the lobed nozzle consisting of 6 lobes in the blowing plane. These troughs are inclined  $22^\circ$  inwards. The nozzle has a diameter of 46 mm and a length of 90 mm. The lobes are with wider openings whose width of each is 6 mm and the height is 10 mm. The initial temperature of the air at the blowing orifice is  $71^\circ\text{C}$ , and its initial axial velocity is  $8\text{ m}\cdot\text{s}^{-1}$ .

### 3 Temperature measurement

The temperatures have not been recorded as long as they are not stable. The reduced temperature ( $T_r$ ) is obtained with reference to the difference of the maximal mean temperature, at the outlet of the blowing orifice, and the ambient temperature. With reference

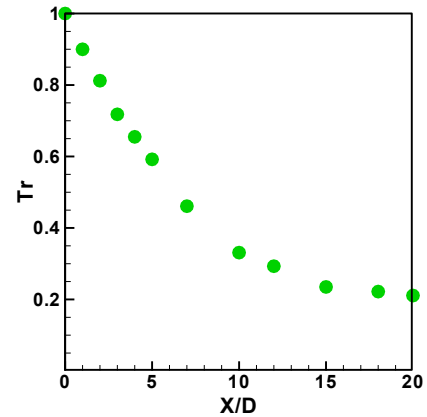


Fig. 3. Axial temperature profile of the free lobed air jet.

to the difference of the maximal mean temperature, at the outlet of the blowing orifice, and the ambient temperature.

$$T_r = \frac{T_i - T_a}{T_{\max} - T_a}. \quad (1)$$

The temperatures ( $T_i$ ) and ( $T_a$ ) have been measured with thermal probes of a precision of 5%.

## 4 Results and discussion

### 4.1 Experimental axial temperature profile of the free lobed jet

The reduced temperature profile ( $T_r$ ) of a lobed air jet is shown in Figure 3.

Figure 3 shows the axial distribution of the reduced temperature ( $T_r$ ) at an axial distance of 20 equivalent diameters for a single lobed jet. The axial temperature profile exhibits Gaussian shapes throughout the jet thereby proving that the temperature stability appears far away from the blowing orifice. We noticed that the axial temperature reached its maximum at  $1D$ , very near to the blowing orifice, then it decreases sharply to attain nearly the  $2/3$  of its initial value at  $7D$ . From the axial station  $7D$  up to  $15D$ , there is a second slope more or less accentuated than the first. Beyond the 15 equivalent diameters, the temperature intensity becomes low and regular along the flow. This result enables to quantify the relative importance of the inclination of the trough relative to the lobed geometry of the blowing plane. This rapid decrease in the axial temperature demonstrates the energy transfer to the radial direction.

### 4.2 Experimental radial temperature profiles of a free lobed jet

Here, we depict (Fig. 4) the radial temperature profiles for different axial stations, namely  $X/D = 1, 2, 3, 5, 7, 10, 15,$  and  $20$ .

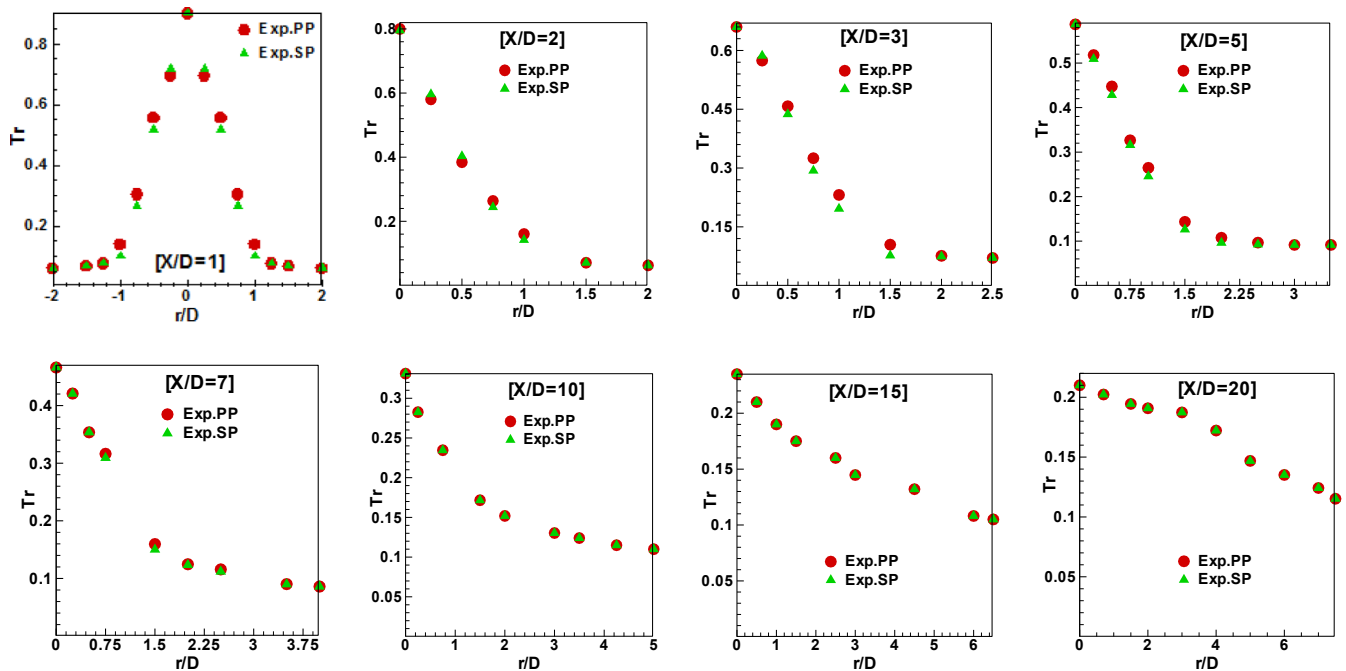


Fig. 4. Radial temperature profiles of a free lobed jet.

#### 4.2.1 Principal and secondary plans

Explicitly, Figure 4 compares the radial temperature profiles in the main plane (denoted by the line joining two lobes standing face to face) and secondary plane (indicated by the line joining two troughs standing face to face) for a free lobed jet.

The inspection of the results obtained shows that, for the same plane (principal or secondary), the flow is axisymmetric indicating the same transfer rate in all directions. Moreover, Figure 4 shows this clearly for the station  $X/D=1$ .

In the symmetry plane of the considered configuration (Fig. 4), we note that the temperature decreases rapidly in the radial direction from a maximum value close to the jet axis to a minimum value so as to tend to the ambient temperature  $T_a$ .

From the axial station  $1D$  to the  $7D$ , we remark clearly the influence of the principal plane on the radial expansion of the temperatures. We remark also, a light temperature decrease in the case of the secondary plane. This difference can be explained by the influence of the widening of the lobes opening.

Beyond the 7 equivalent diameters and till  $20D$ , the flow is not influenced by the type of plane. The jet appears like a circular free jet and that is why the temperature profiles are identical while exhibiting the same radial spread for the two main and secondary planes.

## 5 Numerical procedure

In the present study, the numerical method used is based on the finite volume method (FVM) to simulate the flow. It is now well recognized that this approach provides a very good compromise between accuracy and computational

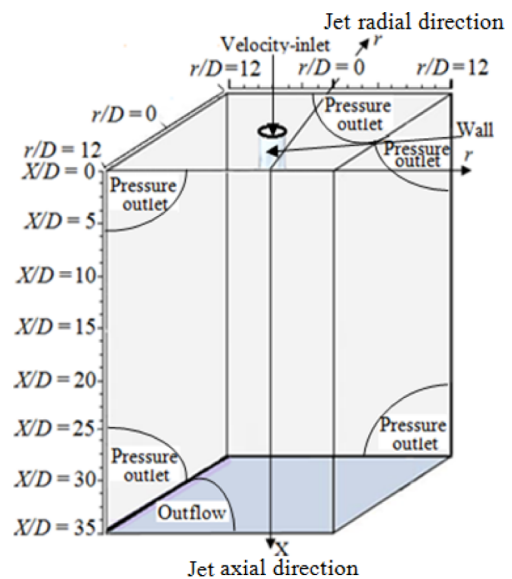


Fig. 5. Computation domain and working stress.

efficiency when simulating most the flows. It should be pointed out that this approach deals with all the equations, namely the discretized unsteady Navier–Stokes equations to which are added the energy and turbulent quantities equations. A two-equation turbulence model and the RSM model, with or without damping functions, represent one of the most popular turbulence closures. The adopted formulations are: (1) a standard  $k-\varepsilon$  model, (2) a RNG  $k-\varepsilon$  model, (3) a SST  $k-\omega$  model, and (4) the Reynolds stress turbulence model (RSM).

Before proceeding with the simulation, it is needful to mesh the considered configuration and specify the suitable BCs.

**Table 1.** RNG  $k$ - $\varepsilon$  model Constants.

$C_\mu$	$C_{1\varepsilon}$	$C_{2\varepsilon}$	$\eta_0$	$\beta$
0.085	1.42	1.68	4.38	0.012

### 5.1 Finite volume method

A key property of FVMs is that conservation principles, which are the basis for the mathematical modeling of continuum mechanical problems, are also fulfilled for discrete equations (conservativity). To be brief, this approach is based on the discretization technique, through control volumes, which converts partial differential equations into algebraic equations, which can then be solved numerically [21].

### 5.2 Mathematical model

The equations governing the flow are the continuity equation, the Reynolds-averaged Navier–Stokes (RANS) equations, and the energy equation, which express the conservation of mass, momentum, and energy, respectively [21].

- Continuity equation:

$$\frac{\partial U_i}{\partial x_i} = 0. \quad (2)$$

- Reynolds-averaged Navier–Stokes (RANS) equations:

$$\rho \frac{\partial}{\partial x_j} (U_i U_j) = -\frac{\partial P}{\partial x_i} + \frac{\partial}{\partial x_j} \left[ \mu \left( \frac{\partial U_i}{\partial x_j} + \frac{\partial U_j}{\partial x_i} \right) - \overline{\rho u'_i u'_j} \right]. \quad (3)$$

- Energy equation:

$$\frac{\partial}{\partial x_i} [u_i (\rho E + p)] = \frac{\partial}{\partial x_j} \left[ \left( k + \frac{C_p \mu_t}{Pr_t} \right) \frac{\partial T}{\partial x_j} + u_i (\tau_{ij})_{eff} \right] + S_h. \quad (4)$$

The Reynolds stress terms appearing in equation (3) represent the diffusive transport of momentum by turbulent motion. These terms need to be determined by a turbulence model before the mean flow equations can be solved. The solution of the equation system above requires the incorporation of appropriate BCs for each variable.

### 5.3 Considered turbulence models

#### 5.3.1 The standard $k$ - $\varepsilon$ model (SKE)

The  $k$ - $\varepsilon$  model is now considered as the standard turbulence model for engineering simulation of flows. It is based on the Boussinesq eddy viscosity model [22], which introduces a turbulent viscosity  $\mu_t$  or eddy viscosity such that:

$$-\overline{\rho u'_i u'_j} = \mu_t \left( \frac{\partial U_i}{\partial x_j} + \frac{\partial U_j}{\partial x_i} \right) - \frac{2}{3} \left( pk + \mu_t \frac{\partial U_k}{\partial x_k} \right) \delta_{ij}, \quad (5)$$

**Table 2.** Tested meshes.

Meshing number	Cell number
Mesh1	633268
Mesh2	1128214
Mesh3	1702062
Mesh4	2326082
Mesh5	3301991
Mesh6	4089508

where  $k$  is the turbulent kinetic energy defined by:

$$k = \frac{1}{2} u'_i u'_i. \quad (6)$$

The turbulent viscosity  $\mu_t$  can be expressed via the following relationship:

$$\mu_t = \rho C_\mu \frac{k^2}{\varepsilon}, \quad (7)$$

with  $C_\mu = 0.09$  (empirical constant), and  $\varepsilon$  being the turbulence dissipation rate.

The equation (7) implies  $k$  and  $\varepsilon$ , which have their own transport equations that can be modeled as follows:

$$\frac{\partial}{\partial x_i} (\rho u_i k) = \frac{\partial}{\partial x_j} \left[ \left( \mu + \frac{\mu_t}{\sigma_k} \right) \frac{\partial k}{\partial x_j} \right] + G_k + G_b - \rho \varepsilon - Y_M + S_k, \quad (8)$$

$$\frac{\partial}{\partial x_i} (\rho u_i \varepsilon) = \frac{\partial}{\partial x_j} \left[ \left( \mu + \frac{\mu_t}{\sigma_\varepsilon} \right) \frac{\partial \varepsilon}{\partial x_j} \right] + C_{1\varepsilon} \frac{\varepsilon}{k} (G_k + C_{3\varepsilon} G_b) - C_{2\varepsilon} \rho \frac{\varepsilon^2}{k} + S_\varepsilon, \quad (9)$$

with  $C_{1\varepsilon} = 1.44$  and  $C_{2\varepsilon} = 1.92$  are empirical constants,  $\sigma_k = 1.0$  and  $\sigma_\varepsilon = 1.3$  are Prandtl numbers for  $k$  and  $\varepsilon$ , respectively,  $S_k$  and  $S_\varepsilon$  are source terms for  $k$  and  $\varepsilon$ , respectively, and  $G_k$  is the generation's term of the turbulent kinetic energy due to the average velocity gradients.

$$G_k = \mu_t \left( \frac{\partial U_j}{\partial x_i} + \frac{\partial U_i}{\partial x_j} \right) \frac{\partial U_j}{\partial x_i}. \quad (10)$$

$G_b$  is the generation term of the turbulence due to buoyancy:

$$G_b = -g_i \frac{\mu_t}{\rho \sigma_h} \frac{\partial \rho}{\partial x_i}. \quad (11)$$

#### 5.3.2 The RNG $k$ - $\varepsilon$ model

The RNG  $k$ - $\varepsilon$  model has a similar form to the SKE [23]. Such a model introduces an additional term into the turbulent dissipation rate  $\varepsilon$ , equation which makes the model more accurate and reliable for a wider class of flows than is the SKE turbulence model (for example, for rapidly strained or swirling flows).

As aforementioned, the two RNG  $k$ - $\varepsilon$  equations are generalizations of the SKE model equations, and can be written down as.

$$\frac{\partial}{\partial x_i} (\rho k U_i) = \frac{\partial}{\partial x_j} \left[ \alpha_k \mu_{eff} \frac{\partial k}{\partial x_j} \right] + G_k + G_b - \rho \varepsilon - Y_M + S_k, \quad (12)$$

$$\begin{aligned} \frac{\partial}{\partial x_i} (\rho \varepsilon U_i) &= \frac{\partial}{\partial x_j} \left[ \alpha_\varepsilon \mu_{eff} \frac{\partial \varepsilon}{\partial x_j} \right] + C_{1\varepsilon} \frac{\varepsilon}{k} (G_k + C_{2\varepsilon} G_b) \\ &\quad - C_{2\varepsilon} \rho \frac{\varepsilon^2}{k} - R_\varepsilon + S_\varepsilon. \end{aligned} \quad (13)$$

The main difference between the RNG and standard  $k$ - $\varepsilon$  models lies in the additional term  $R_\varepsilon$  (Eq. (13)), which it can be expressed as:

$$R_\varepsilon = \frac{C_\mu \rho \eta^3 \left(1 - \frac{\eta}{\eta_0}\right) \varepsilon^2}{1 + \beta \eta^3} \frac{1}{k}, \quad (14)$$

where  $\eta_0 = 4.38$ ,  $\beta = 0.012$ ,  $\eta = Sk/\varepsilon$ , and  $S = (2S_{ij} S_{ij})^{1/2}$  with  $S_{ij} = \frac{1}{2} \left( \frac{\partial U_i}{\partial x_j} + \frac{\partial U_j}{\partial x_i} \right)$ , which is the mean strain rate tensor.

Using the equation (14), the equation (13) becomes:

$$\frac{\partial}{\partial x_i} (\rho \varepsilon U_i) = \frac{\partial}{\partial x_j} \left[ \alpha_\varepsilon \mu_{eff} \frac{\partial \varepsilon}{\partial x_j} \right] + C_{1\varepsilon} \frac{\varepsilon}{k} (G_k + C_{2\varepsilon} G_b) - C_{2\varepsilon}^* \rho \frac{\varepsilon^2}{k}, \quad (15)$$

where  $C_{2\varepsilon}^*$  is given by:

$$C_{2\varepsilon}^* = C_{2\varepsilon} + \frac{C_\mu \eta^3 \left(1 - \frac{\eta}{\eta_0}\right)}{1 + \beta \eta^3}. \quad (16)$$

The constants of the model are given in Table 1.

### 5.3.3 Reynolds stress model (RSM)

The Reynolds stress model is based on the second-moment closure. The starting point for the development of RSM is the exact differential transport equation for the Reynolds stresses. In this model, the Reynolds constraints are calculated using their own transport equations while avoiding the concept of turbulent (isotropic) viscosity. In other words, this model involves the individual calculation of each stress  $\overline{u_i u_j}$ . These equations are used to close the averaged Reynolds equation system for the transport of the moment equation [23]. It should be noted that simplifying hypothesis for the modeling of the unknown terms is necessary. Thereby, the retained model is briefly outlined herein after:

The transport equations of the Reynolds stresses can be written as follows:

$$\begin{aligned} \underbrace{\frac{\partial}{\partial x_k} (\rho u_k \overline{u_i u_j})}_{C_{ij} \equiv \text{Convection}} &= - \underbrace{\frac{\partial}{\partial x_k} [\rho \overline{u_i u_j u_k} + p(\delta_{kj} u_i + \delta_{ik} u_j)]}_{D_{T,ij} \equiv \text{Turbulent Diffusion}} \\ &\quad + \underbrace{\frac{\partial}{\partial x_k} \left[ \mu \frac{\partial}{\partial x_k} \overline{u_i u_j} \right]}_{D_{L,ij} \equiv \text{Molecular Diffusion}} - \underbrace{\rho \left[ \overline{u_i u_k} \frac{\partial u_j}{\partial x_k} + \overline{u_j u_k} \frac{\partial u_i}{\partial x_k} \right]}_{p_{ij} \equiv \text{Stress Production}} \\ &\quad - \underbrace{\rho \beta (g_i \overline{u_j \theta} + g_j \overline{u_i \theta})}_{G_{ij} \equiv \text{Buoyancy Production}} + \underbrace{p \left( \frac{\partial u_i}{\partial x_j} + \frac{\partial u_j}{\partial x_i} \right)}_{\phi_{ij} \equiv \text{Pressure Strain}} \end{aligned}$$

$$\begin{aligned} &\quad - 2 \underbrace{\mu \frac{\partial u_i}{\partial x_k} \frac{\partial u_j}{\partial x_k}}_{\varepsilon_{ij} \equiv \text{Dissipation}} - \underbrace{2 \rho \Omega_\kappa (\overline{u_j u_m} \varepsilon_{ikm} + \overline{u_i u_m} \varepsilon_{jkm})}_{F_{ij} \equiv \text{Production by System Rotation}} \\ &\quad + \underbrace{S_{user}}_{\text{user-Defined Source Term}} \end{aligned} \quad (17)$$

Of the various terms in these exact equations,  $C_{ij}$ ,  $D_{L,ij}$ ,  $P_{ij}$ , and  $F_{ij}$  do not require any modeling. However,  $D_{T,ij}$ ,  $G_{ij}$ ,  $\phi_{ij}$ , and  $\varepsilon_{ij}$  need to be modeled to close the equations. The following sections describe the modeling assumptions required to close the equation set.

The generalized gradient diffusion hypothesis is the most popular model for  $D_{T,ij}$ , though often for simplicity, which is also the case here, the isotropic model of the turbulent diffusion is adopted:

$$D_{T,ij} = \frac{\partial}{\partial x_k} \left( \frac{\mu_t}{\sigma_k} \frac{\partial u_i u_j}{\partial x_k} \right). \quad (18)$$

The scalar turbulent dissipation rate  $\varepsilon$  is computed from a transport equation analogous to the  $k$ - $\varepsilon$  model:

$$\frac{\partial}{\partial x_i} (\rho U_i \varepsilon) = \frac{\partial}{\partial x_j} \left[ \left( \mu + \frac{\mu_t}{\sigma_t} \right) \frac{\partial \varepsilon}{\partial x_j} \right] + C_{\varepsilon 1} \frac{P_{ii} \varepsilon}{2k} - C_{\varepsilon 2} \rho \frac{\varepsilon^2}{k}, \quad (19)$$

Note that the Reynolds stresses values at the inlet are determined approximately by specific values of  $k$ .

### 5.3.4 The SST $k$ - $\omega$ turbulence model

Another popular two-equations model pairs  $k$  with the specific dissipation rate ( $\omega$ ). It mainly aims to model near-wall interactions more accurately than  $k$ - $\varepsilon$  models. One variant of  $k$ - $\omega$  that has gained popularity, especially in the aeronautics area, is the SST model. The model has gained this popularity based on its ability to predict separation and reattachment better when compared to  $k$ - $\varepsilon$  and the standard  $k$ - $\omega$ . The SST  $k$ - $\omega$  has become one of the most widely used turbulence models [24]. This model uses a function  $F_1$  which enables us to pass from the  $k$ - $\omega$  model near the wall to the  $k$ - $\varepsilon$  model far away from it.

$$U_j \frac{\partial k}{\partial x_j} = \frac{\partial}{\partial x_j} \left[ \left( \nu + \frac{\nu_t}{\sigma_k} \right) \frac{\partial k}{\partial x_j} \right] - \beta^* k \omega_k + \nu_t S^2, \quad (20)$$

$$\begin{aligned} U_j \frac{\partial \omega}{\partial x_j} &= \frac{\partial}{\partial x_j} \left[ \left( \nu + \frac{\nu_t}{\sigma_\omega} \right) \frac{\partial \omega}{\partial x_j} \right] - \gamma S^2 - \beta f_\beta \omega^2 \\ &\quad + 2 \sigma_{\omega^2} (1 - F_1) \frac{1}{\omega}. \end{aligned} \quad (21)$$

The coefficients  $\varphi$  ( $= \sigma_k, \sigma_\omega, \gamma, \beta$ ) are interpolated using the following formula:

$$\varphi = F_1 \varphi_1 + (1 - F_1) \varphi_2. \quad (22)$$

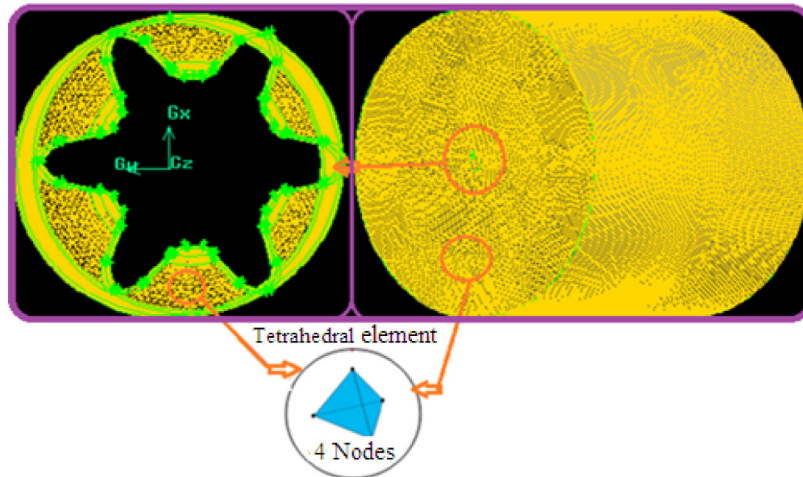


Fig. 6. Meshing of the computation domain.

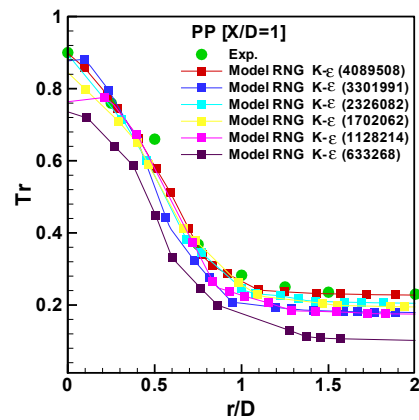
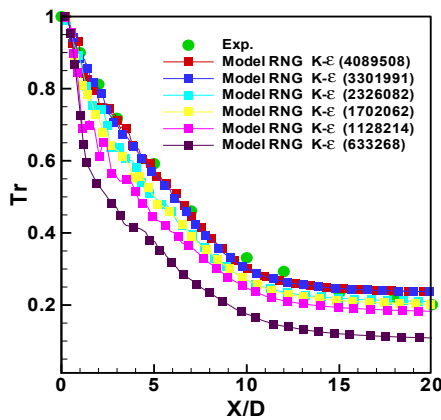


Fig. 7. Independence of the solution (axial temperature) with respect to the mesh.

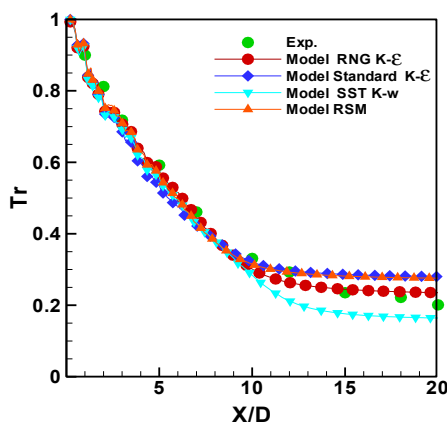


Fig. 9. Comparison of the experimental and numerical temperature in the axial direction.

The coefficient  $\varphi_1$  is that of the  $k-\omega$  model (boundary layer: viscous sub-layer, buffer region, logarithmic layer), whereas the coefficient  $\varphi_2$  is that of the  $k-\epsilon$  model (outside the boundary layer). Note that the  $F_1$  function is

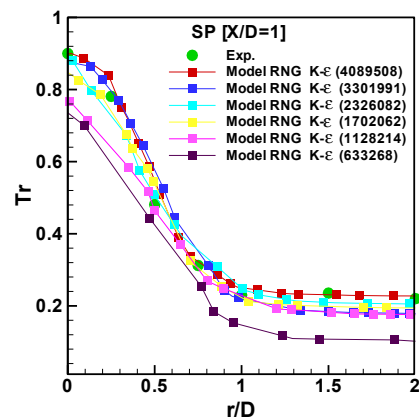


Fig. 8. Independence of the solution (radial temperature) with respect to the mesh at  $X/D=1$ .

equal to 1 in the boundary layer and 0 outside. Further, the Bradshaw [25] hypothesis is used here to limit the turbulent viscosity in regions with adverse pressure gradients:

$$\nu_t = \frac{a_1 k}{\max(a_1 \omega; F_2 \bar{\Omega})},$$

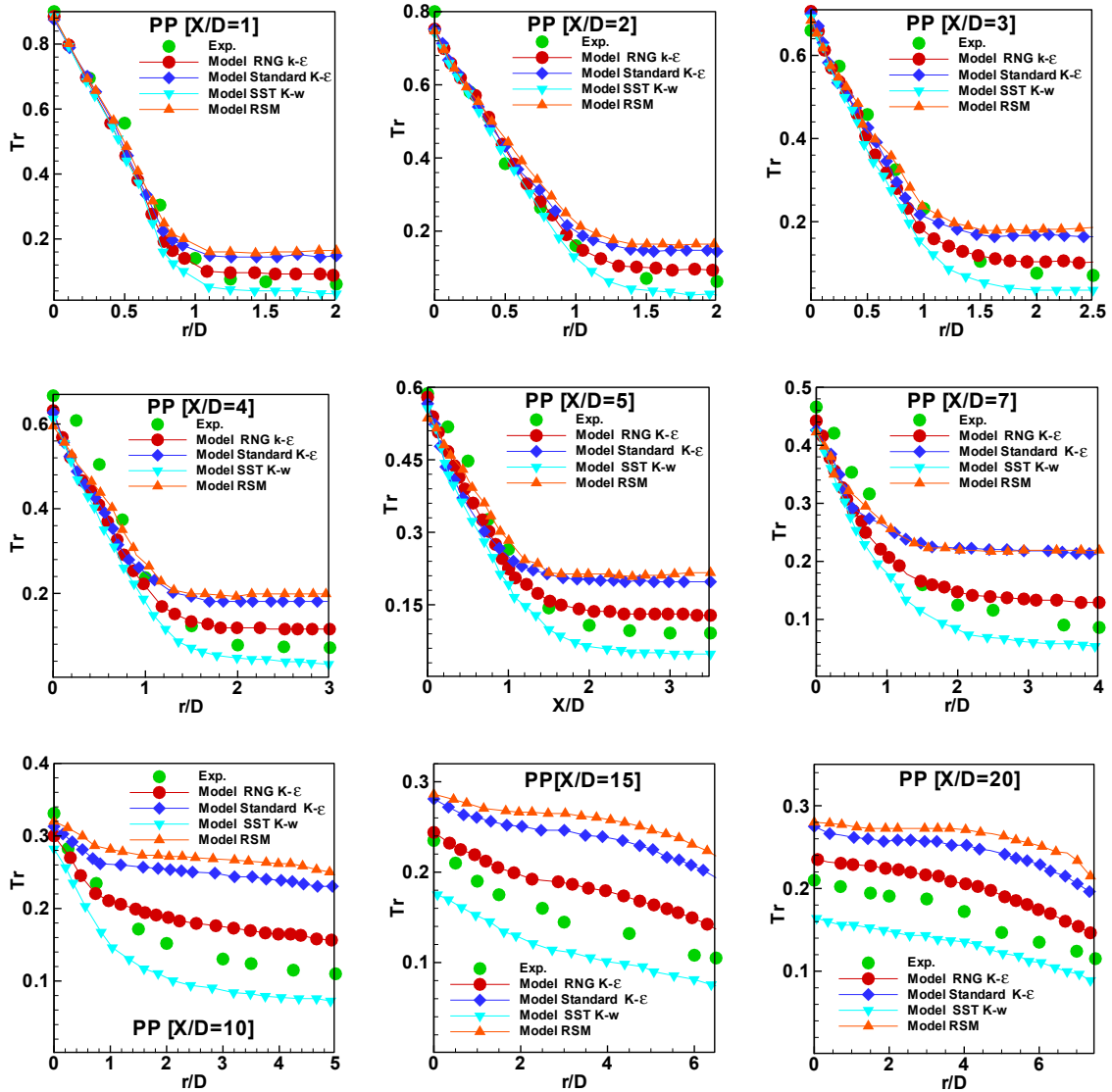


Fig. 10. Comparison of the experimental and numerical radial temperature profiles (principal plane).

$$\text{where } \overline{\Omega} = \sqrt{2\Omega_{ij}\Omega_{ij}}$$

$$\text{and } \Omega_{ij} = \frac{1}{2} \left( \frac{\partial U_j}{\partial x_j} - \frac{\partial U_j}{\partial x_i} \right),$$

where the Bradshaw constant ( $a_1$ ) is equal to 0.31. The Bradshaw correction [25] is applied in the boundary layer (where  $F_2 = 1$ ), and outside the boundary layer we used the relation  $v_t = k/\omega$  (where  $F_2 = 0$ ).

#### 5.4 Boundary conditions (BCs)

The suitable BCs are presented in Figure 5. The room dimensions are very large compared to those of the zone of air diffusion.

The BCs for the considered turbulence models SST  $k-\omega$ ,  $k-\epsilon$  standard, RNG  $k-\epsilon$ , and the RSM model are as follows:

- velocity inlet:  $8 \text{ (m}\cdot\text{s}^{-1})$ ;
- temperature inlet:  $71 \text{ (}^\circ\text{C)}$ ;
- turbulence intensity: 5 (%);
- relaxation factors: pressure = 0.3, density = 0.9, energy = 0.9, moment = 0.6, body forces = 0.9, turbulent kinetic energy = 0.7, specific dissipation rate = 0.7, turbulent viscosity = 0.9.
- convergence criteria: energy =  $10^{-7}$ , other quantities =  $10^{-4}$ ;
- Reynolds number:  $Re = 18330$ ;
- pressure: standard.

#### 5.5 Grid independence

For the 3D study carried out, we set out the simulation results obtained using the “Fluent” code associated with the package Gambit mesh software [26], which generates the grid for the simulated domain. Likewise, we optimised, the mesh convenient for our study (see Fig. 6). The results have been validated by comparison with those obtained experimentally.

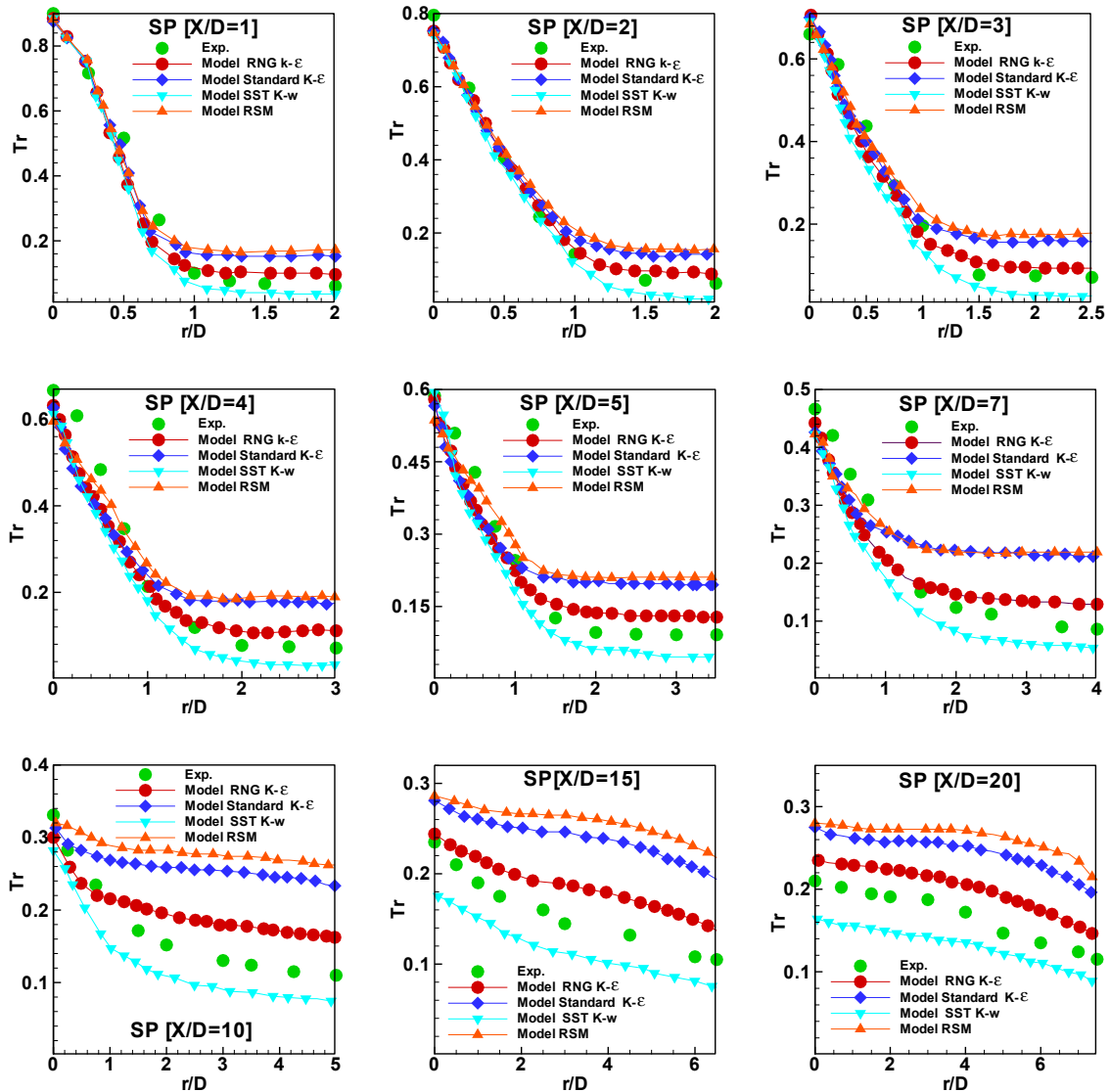


Fig. 11. Comparison of the experimental and numerical radial temperature profiles (secondary plane).

It is the model RNG  $k-\epsilon$  which has been tested with several meshes (Tab. 2) to investigate their effects.

From Figures 7 and 8, we observe that the axial and radial temperature profiles do not vary substantially with the mesh. Consequently, the mesh 5 (see Tab. 2) which demonstrates the least mesh dependence is used for all following simulations.

## 5.6 Validation and results

### 5.6.1 Reduced axial temperature profiles (lobed jet case)

The Figure 9 presents a comparison between the experimental and numerical results relating to the reduced axial temperature ( $T_r$ ) at different stations. The numerical results are obtained by means of the four turbulence models: SST  $k-\omega$ ,  $k-\epsilon$  standard, RNG  $k-\epsilon$ , and the RSM.

Through this figure, a good agreement between the predicted and measured temperatures is clearly observed in the region close to the blowing orifice

(potential core region). Only the SST  $k-\omega$  model exhibits a difference from  $X/D=10$  (region where the flow is fully developed) where the temperature starts to decrease significantly.

To sum up, it seems that, among the turbulence models assessed, it is the model RNG  $k-\epsilon$  which provides values which corroborate the experimental measurements.

### 5.6.2 Reduced radial temperature profiles of a lobed jet

#### 5.6.2.1 Reduced radial temperature profile in the principal plane

Figures 10 and 11 depict the predicted radial temperature profiles (with the RNG  $k-\epsilon$ ,  $k-\epsilon$  standard, SST  $k-\omega$ , and the RSM turbulence models) compared to the experimental results at the stations ( $X/D=1, 2, 3, 4, 5, 7, 10, 15,$  and  $20$ ), this is, for the principal and secondary plane.

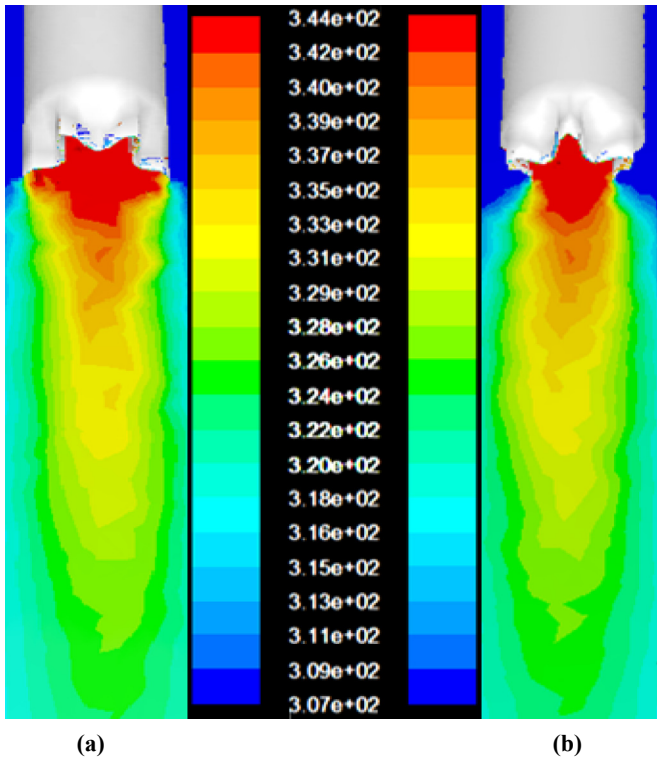


**Fig. 12.** Temperature contours, (a) principal plane, (b) secondary plane.

A thorough inspection of these figures shows that our simulation findings with the RNG  $k-\varepsilon$  and SST  $k-\omega$  models corroborate the experimental results, unlike the  $k-\varepsilon$  standard and RSM models. In the light of the results obtained, it appears that it is the model RNG  $k-\varepsilon$  which seems the most efficient for both the main and secondary planes.

### 5.6.3 Temperature contours

Figure 12a and b plot temperature contours in the principal and secondary planes, respectively.

The temperatures of the lobed jet decrease through the flow, particularly in the potential core region. This behavior is confirmed by the experimental results at different axial and radial distances for the principal and secondary plane. The analysis of these figures shows that the radial temperatures are not homogeneous near the blowing device. They start to be after a certain axial and radial distance from the jet outlet surface. This behavior confirms the influence of both the lobes and troughs shapes that enable a relative jet expansion in the principal plane comparing to the secondary one, this is done, before the station  $X/D=7$  (potential core region). Beyond this value (transition zone), the lobed jet behaves like a circular one.

## 6 Conclusion

This study dealt with an experimental and numerical investigation of a jet from a lobed diffuser to assess its performance in terms of homogenization of such an environment.

Based on the findings' analyses, the following conclusions can be drawn:

- in the potential core region, the thermal profiles are more spread out in the principal plane because of the effect of the wider opening of the lobes;
- in transition and fully developed zones, the temperature profiles are not influenced by the lobes and troughs shapes, and then the jet will be similar to the circular one;
- it appears that the temperature profiles predicted by the RNG  $k-\varepsilon$  and SST  $k-\omega$  models are in good agreement with the experimental results, unlike those predicted by the models  $k-\varepsilon$  standard and RSM. However, it turned out that no model can simultaneously predict thermal characteristics in the principal and secondary planes due to the tridimensional character of the flow;
- the results obtained show that the jet considered here is suitable for residential heating and air-conditioning applications.

## Nomenclature

$Ar$	Archimedes number, $Ar = gL_c^3\rho(\rho_b - \rho)/\mu^2$
$C_p$	specific heat capacity ( $\text{J}\cdot\text{kg}^{-1}\cdot\text{C}^\circ$ )
$D$	equivalent diameter, m
$g_i$	acceleration due to gravity ( $\text{m}\cdot\text{s}^{-2}$ )
$G_x$	axial pushing force ( $\text{kg}\cdot\text{m}^2\cdot\text{s}^{-2}$ )
$H$	lobe height (m)
$k$	turbulent kinetic energy ( $\text{m}^2\cdot\text{s}^{-2}$ )
$L$	lobe length, m
$L_c$	body characteristic length (m)
$P$	pressure in the jet cross-section (Pa)
$P_{ij}$	production term of the Reynolds stresses
$PP$	principal plane
$R_\varepsilon$	additional term (Eq. 14)
$Re$	Reynolds number
$S$	swirl number
$S_k, S_\varepsilon$	source terms
$SP$	secondary plane
$r/D$	dimensionless radius (radial direction)
$X/D$	dimensionless height (axial direction) due to the mean velocity gradient
$T_a$	ambient temperature ( $^\circ\text{C}$ )
$T_i$	jet temperature at different points ( $^\circ\text{C}$ )
$T_{max}$	blowing temperature ( $^\circ\text{C}$ )
$T_r$	reduced temperature
$u$	velocity component in the x-direction
$Y_M$	contribution of the fluctuating dilatation in compressible turbulence to the overall dissipation rate

## Greek symbols

$\alpha_{ext}$	exterior angle of the lobes ( $^\circ$ )
$\alpha_{int}$	interior angle of the lobes ( $^\circ$ )
$\alpha_k, \alpha_\varepsilon$	inverse effective Prandtl number for $k$ and $\varepsilon$ , respectively
$\varepsilon$	turbulent kinetic energy dissipation rate ( $\text{m}^2\cdot\text{s}^{-3}$ )
$\delta_{ij}$	Kronecker's tensor
$\eta$	mean flow rate deformation
$\mu$	dynamic viscosity ( $\text{kg}\cdot\text{m}^{-1}\cdot\text{s}^{-1}$ )
$\nu$	Kinematic viscosity ( $\text{m}^2\cdot\text{s}^{-1}$ )

$\nu_t$	turbulent Kinematic viscosity ( $\text{m}^2\cdot\text{s}^{-1}$ )
$\rho$	fluid density ( $\text{kg}\cdot\text{m}^{-3}$ )
$\rho_b$	body density ( $\text{kg}\cdot\text{m}^{-3}$ )
$\sigma_k, \sigma_\varepsilon$	turbulent Prandtl numbers associated to $k$ and $\varepsilon$ , respectively
$(\tau_{ij})_{eff}$	deviatoric stress tensor

## References

- [1] A. Dia, Simulation de jets d'air lobés pour l'optimisation des Unités Terminales de Diffusion d'Air, Doctorat en sciences, Université de la Rochelle, 2012
- [2] P.E. Dimotakis, The mixing transition in turbulent flows, *J. Fluid Mech.* 409 (2000) 68–69
- [3] A. Meslem, I. Nastase, F. Allard, Passive mixing control for innovative air diffusion terminal devices for buildings, *Build. Environ.* 45 (2010) 2679–2688
- [4] A. Meslem, M. Elhassan, I. Nastase, Analysis of jet entrainment mechanism in the transitional regime by time-resolved PIV, *J. Vis.* 14 (2011) 41–52
- [5] M. Elhassan, A. Meslem, K. Abed-Meraïm, Experimental investigation of the flow in the near-field of a cross-shaped orifice jet, *Phys. Fluids* 23 (2011) 1–16
- [6] I. Nastase, A. Meslem, V. Iordach, I. Colda, Lobed grilles for high mixing ventilation – an experimental analysis in a full scale model room, *Build. Environ.* 46 (2011) 547–555
- [7] A. Meslem, F. Bode, I. Nastase, O. Martin, Optimization of lobed perforated panel diffuser: numerical study of orifice geometry, *Mod. Appl. Sci.* 6 (2012) 1–59
- [8] I. Nastase, Analyse des jets lobés en vue de leur intégration dans les Unités Terminales de Diffusion d'air, Thèse de doctorat en science, Université de la Rochelle, 2007
- [9] A. Meslem, I. Nastase, K. Abed-Meraïm, Experimental investigation of the mixing performance of a lobed jet flow, *J. Eng. Phys. Thermophys.* 81 (2008) 106–111
- [10] I. Nastase, A. Meslem, Vortex dynamics and mass entrainment in turbulent lobed jets with and without lobe deflection angles, *Exp. Fluids* 48 (2010) 693–714
- [11] M. El Hassan, A. Meslem, Time-resolved stereoscopic particle image velocimetry investigation of the entrainment in the near field of circular and daisy-shaped orifice jets, *Phys. Fluids* 22 (2010) 35–107
- [12] A. Meslem, A. Dia, C. Beghein, M. El Hassan, I. Nastase, P. J. Vialle, A comparison of three turbulence models for the prediction of parallel lobed jets in perforated panel optimization, *Build. Environ.* 46 (2011) 2203–2219
- [13] Y. Yuan, Jet fluid mixing control through manipulation of inviscid flow structures, PhD Thesis, Virginia Polytechnic Institute and State University, 2000
- [14] H. Hu, T. Kobayashi, T. Saga, S. Segawa, N. Taniguchi, Particle image velocimetry and planar laser-induced fluorescence measurements on lobed jet mixing flows, *Exp. Fluids* 29 (2000) 141–157
- [15] H. Hu, T. Kobayashi, N. Taniguchi, A study on a lobed jet mixing flow by using stereoscopic particle image velocimetry technique, *Phys. Fluids* 13 (2001) 25–34
- [16] A. Bennia, L. Loukarfi, A. Khelil, M. Braikia, S. Rahal, Y. Bouhamidi, Jet turbulent à diffuseur muni de lobes: application au confort dans les locaux à usage d'habitation, *Rev. Nat. Technol. C- Sci. Environ.* 13 (2015) 34–38
- [17] A. Bennia, L. Loukarfi, M. Braikia, A. Khelil, H. Naji, Etude expérimentale d'un jet turbulent à diffuseur muni de lobes: Application au confort dans les locaux à usage d'habitation, *Rev. Nat. Technol. A- Sci. Fondam. Eng.* 13 (2015) 54–58
- [18] A. Meslem, I. Nastase, O. Martin, Sur la validation expérimentale des modèles de turbulence. Application à un jet d'air lobé, in: XXXe Rencontres AUGC-IBPSA, 2012
- [19] A. Meslem, F. Bode, C. Croitoru, I. Nastase, Comparison of turbulence models in simulating jet flow from a cross-shaped orifice, *Eur. J. Mech.* 44 (2014) 100–120
- [20] M. Braikia, L. Loukarfi, A. Khelil, A. Naji, Improvement of thermal homogenization using multiple swirling jets, *Therm. Sci.* 16 (2012) 239–250
- [21] A. Bennia, S. Rahal, La convection naturelle dans une cavité simulante un thermosiphon, Editions Universitaires Européennes, 2014, pp. 1–140
- [22] B.D. Pratte, J.R. Keffer, The swirling turbulent jet, *J. Int. Eng. Trans. J.S.M.E.* (1972) 739–748.
- [23] D. Choudhury, Introduction to the renormalization group method and turbulence modeling, Fluent Inc, Technical Memorandum, TM-107, 1993
- [24] F.R. Menter, Zonal two equation  $k-\omega$  turbulence models for aerodynamic flows, AIAA Paper 93-2906, NASA-TM-111629, NAS 1.15:111629, AIAA Paper 93-2906, 1993
- [25] P. Bradshaw, Turbulent secondary flows, *Annu. Rev. Fluid Mech.* 19 (1987) 53–74
- [26] Gambit, A CFD preprocess gambit 2.0 User's Guide, USA, 2002

**Cite this article as:** A. Bennia, L. Loukarfi, A. Khelil, S. Mohamadi, M. Braikia, H. Naji, Experimental and numerical investigation of a turbulent lobed diffuser jet: application to residential comfort, *Mechanics & Industry* **19**, 104 (2018)